CHAPTER 3

MILO PERFORMANCE IMPROVEMENT USING EQUIVALENT CIRCUIT APPROACH*

3.1 Overview

3.2 Introduction

3.3 Analysis

- **3.3.1 Tapering Toward Input Side of Cathode**
- **3.3.2 Tapered Choke Section**
- **3.3.3 Impedance Matching at the Extractor Section**
- **3.3.4 Stub Position Optimization**

3.4 Results And Discussion

- **3.4.1 Optimization of Tapering Length of Cathode at Input Side**
- **3.4.2 Optimization of Tapered Choke Section**
- **3.4.3 Optimization of Extractor Section**
- **3.4.4 Optimization of Stub Position**
- **3.4.5 Simulation Results**

3.5 Conclusion

*Part of this work has been published as:

Arjun Kumar, Smrity Dwivedi, and P. K. Jain, "MILO Performance Improvement Study—An Equivalent Circuit Approach," *IEEE Transactions on Plasma Science,* vol. 47, no. 10, pp. 4542-4649, 2019.

3.1. Overview

In this Chapter, an HPM oscillator MILO design study has been carried out to improve its performance. Impedances of the different sub-sections of the device have been matched. An equivalent circuit approach, which is simpler and easy to handle, has been adopted for this purpose. First, the input impedance of the tapered inner conductor of the coaxial structure has been matched with the impedance of the choke discs. Then the extractor inner radius and extractor gap impedance have been optimized at the output section. This impedance matching scheme provides the maximum efficiency of the device with maximum RF transmission. The optimum position of the stub to match the impedance with the output side has also been analyzed. To validate our concept, initially an experimentally reported *L*-band MILO has been simulated using commercial PIC code which provides an RF output power of 1.38 GW with an efficiency of 7.8%. The PIC simulation results have been found in agreement of ~ 5% with the experimental values. Further, the PIC simulation with the optimized design parameters has improved the RF output power of 2.5 GW with an efficiency of 14.4%.

3.2. Introduction

High Power Microwave (HPM) sources are extensively required for HPM systems for various applications in the fields of space, energy, environment, and defence [Benford *et al.* (2007)]. Magnetically insulated line oscillator (MILO) is one of the low impedance HPM source, which is compact, simple, and does not require an external DC magnetic field for electrons bunch focusing. The other conventional HPM oscillators, like, relativistic BWO and relativistic magnetron require an external DC magnetic field

which makes the system heavier and complicated. Vircator is another simple high peak-power HPM source; however, it finds limited application in the systems due to low efficiency. MILO is a slow-wave cross-field HPM oscillator that generates RF power in GW level ranging from *L*-band to *Ku*-band and its self-magnetic insulation mechanism makes the device compact and lightweight [Lemke *et al.* (1997)]. MILO employs a disc-loaded metallic coaxial waveguide as its RF interaction structure. A choke structure at its input side prevents the leakage of RF waves toward the DC pulser. An extractor section at the end of its RF interaction structure converts the standing wave into the traveling wave for energy flow. The last sub-section of the device contains matching stubs along with a beam dump to couple out RF power generated and collects the unspent electrons.

Beam-wave interaction and magnetic insulation mechanism analyses for the MILO device have been performed by several authors [Lemke *et al.* (1990), Lemke *et al.* (1997), Eastwood *et al.* (1998), Dwivedi and Jain (2014), Cousin *et al.* (2007), Haworth *et al.* (2000), Haworth *et al.* (2002) and Fan *et al.* (2007)]. Analytical and experimental work related to the RF power extraction has been reported using the stepped transformer impedance matching technique [Lemke *et al.* (1990)]. The stepped tapered extractor discs have been introduced to extract the stored RF by gradual changing of its group velocity [Eastwood *et al.* (1998)]. Dwivedi and Jain have used the tapered SWS structure along with a tapered extractor for performance improvement by impedance matching [Dwivedi and Jain (2014)]. Lemke *et al.* have used load-limited MILO and performed an experimental study of RF power extraction through different extractor disc inner radius [Lemke *et al.* (1997)]. Cousin *et al.* have demonstrated a compact MILO device with modification at the collector side achieves ~6% efficiency

and longer pulse width [Cousin *et al.* (2007)]. With design modification in MILO structure (mainly in cathode design), pulse lengthening along with efficiency enhancement up to 10.6% has been achieved by Haworth *et al.* [Haworth *et al.* (2000) and Haworth *et al.* (2002)]. Fan *et al.* have proposed further modification in MILO design to improve the overall device efficiency up to 12% through the introduction of a beam-dump within its collector [Fan *et al.* (2007)].

Though analytical, simulation, and experimental work on MILO have been explored extensively; however, device performance optimization studies are limited to experimental and simulation studies. In this present chapter, device performance improvement and optimization studies have been carried out analytically. Here, we have adapted an impedance matching approach. Impedances of the different MILO subassemblies are matched to minimize the reflection and maximize the RF power transfer inside the device. For this purpose, an equivalent circuit approach has been used which is easy to handle in comparison to the field analytical approach. To validate our developed analytical approach, resort of PIC simulation is taken to estimate the improved device RF output power and efficiency.

This chapter organizes the work as follows. In section 3.3, the analytical study of impedance matching of different device sub-sections through an equivalent circuit approach is performed. In section 3.4, results and the estimated power generation using a 3D PIC commercial code “CST Particle Studio” is also briefly explained. Section 3.5, presents conclusions drawn about the device performance improvement through impedance matching of its different assemblies.

3.3. Analysis

In this section, the impedance matching of the MILO at different sections of the device is analyzed using the equivalent circuit approach. For this purpose, the characteristic impedance of the structure is calculated using the design parameters of the different device sections (Fig. 3.1). The magnetically insulated line oscillator (MILO) comprises of disc-loaded coaxial structure with different disc-inner radius at the input and output side, having different characteristic impedances. The improvement in device performance can be achieved by matching the impedances of the different device sections from input to output sides. This also helps in maximizing the power transfer from source to load and minimizing the reflection from the load. Here, equivalent circuit analysis is used to analyze the characteristic impedance and dispersion relation of different sections of the MILO device. The MILO device structure uses different distributed line parameters for different sections (i.e. for the choke, RF interaction cavity, and extractor section), characterized by the equivalent shunt capacitance per unit length (i.e. $C_{ch}(z)$, C_{IC}, C_{ex}) and the equivalent series inductance per unit length (i.e. $L_{ch}(z)$, L_{IC}, L_{ex}) considering lossless condition (i.e. equivalent series resistance per unit length *R* and equivalent shunt conductance per unit length *G* are ignored). Fig. 3.1 shows the schematic diagram of MILO with its different sections. MILO device structure can be divided into four sections: section-A as tapered cathode section, section-B as tapered choke section, section-C as RF interaction cavities section, and section-D as extractor section, as shown in Fig. 3.1. Device sections can be further divided into two regions: region *I* and region *II*. The disc-free region is considered as region *I* and disc occupied region is considered as region *II*. The characteristic impedance of the different sections are calculated using structure design parameters,

with r_c as the cathode radius, r_{ai} as inner radius of interaction cavity section disc, r_{ao} as outer radius of the disc, d as the periodicity of disc loading, r_{ch} as inner radius of choke disc, r_{ext} as inner radius of extractor disc, T as the thickness of the disc, l_T cathode tapering length and d_{ex} as extractor gap.

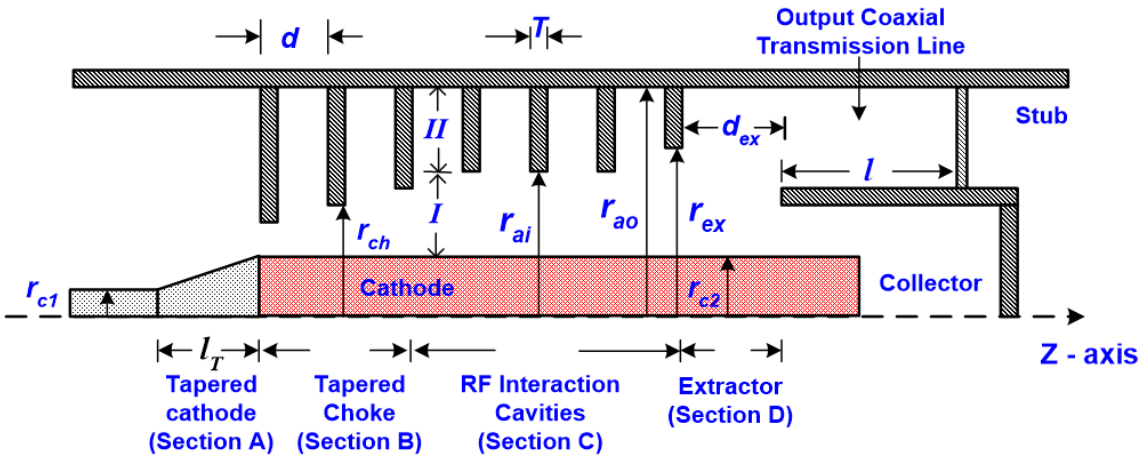

Figure 3.1: Schematic view of the magnetically insulated line oscillator (MILO) structure.

The equivalent series inductance per unit length (L_{IC}) for the RF interaction cavities section can be calculated using voltage telegraphist's equation, as given in [Dixit and Jain (2016)]:

$$L_{IC} = (1/\ j\omega)(\beta_n^I / \gamma_n^I)^2 W_{nm} \tag{3.1}$$

Similarly, The equivalent shunt capacitance per unit length (C_{IC}) for this RF interaction cavities section which is a disc loaded coaxial structure can be calculated using the current telegraphist's equation, as explained in [Dixit and Jain (2016)]:

$$C_{IC} = j(\gamma_n^I)^2 / (\omega P_{nm}) \tag{3.2}$$

Where W_{nm} is the inductance factor and P_{nm} is the capacitance factor and are given as [Dixit and Jain (2016)]:

$$W_{nm} = \frac{F_0\{\gamma_n^I\ r_{ai}\}\gamma_m^{II}\gamma_n^I}{[(j\beta_m^{II}\omega\varepsilon)F_0'\{\gamma_n^I\ r_{ai}\}\gamma_n^I - (j\beta_n^I\omega\varepsilon)\gamma_m^{II}\ F_0'\{\gamma_n^I\ r_c\}]S} \times \frac{\cos(\beta_m^{II}(d-T))}{(2\pi r_{ai})}$$

and,

$$P_{nm} = \frac{\cos(\beta_m^{II}(d-T))\exp(-j\omega t)}{2\pi r_{ai}(j\omega\varepsilon)[P_0]S} \times F_0\{\gamma_n^I r\}F_0\{\gamma_n^I r_{ai}\}Y_0\{\gamma_n^I r_c\}\gamma_m^{II}\gamma_n^I$$

where,

$$P_0 = X_0\{\gamma_m^{II} r_{ai}\}X_0'\{\gamma_m^{II} r_{ai}\}\beta_m^{II}Y_0\{\gamma_n^I r_c\} - \gamma_m^{II}J_1\{\gamma_n^I r_{ai}\}F_0\{\gamma_n^I r_c\}$$

Here, $\beta_n^I\ (=\beta_0^I \pm 2n\pi/d)$ is the axial propagation constant, $\gamma_n^I\ (=(k^2-\beta_n^{I2})^{1/2})$ is the radial propagation constant, $k(=\omega(\mu_0\varepsilon_0)^{1/2})$ is the free space propagation constant, and $n(=0,\pm1,\pm2,\pm3,....)$ is the integer for space harmonics in region *I*. $\beta_m^{II} = m\pi/(d-T)$ is the axial propagation constant for standing wave and $\gamma_m^{II} = (k^2-(\beta_m^{II})^2)^{1/2}$ is the radial propagation constant with $m(=+1,+2,+3,....)$ as modal harmonics present in region *II*. $F_0\{\gamma_n^I r\}$, $F_0'\{\gamma_n^I r\}$ and S are

$$F_0\{\gamma_n^I r\} = Y_0\{\gamma_n^I r_c\}\ J_0\{\gamma_n^I r\} - J_0\{\gamma_n^I r_c\}\ Y_0\{\gamma_n^I r\}$$

$$F_0'\{\gamma_n^I r\} = Y_0\{\gamma_n^I r_c\}\ J_1\{\gamma_n^I r\} - J_0\{\gamma_n^I r_c\}\ Y_1\{\gamma_n^I r\}$$

and, $$S = \left(\frac{2\beta_m^{II}}{d-T}\right)\left(\frac{(-1)^m\exp(j\beta_n^I(d-T))-1}{(\beta_m^{II})^2-(\beta_n^I)^2}\right) \quad .$$

Here, J_0, J_1, Y_0, and Y_1 are the Bessel function of 1st and 2nd kind, respectively.

Subscripts *0* and *1* represent the order of the Bessel function.

The characteristics impedance of the disc-loaded coaxial structure can be defined in usual terms of the distributed line parameters as [Dixit and Jain (2016)]:

$$Z_{IC} = \left(L_{IC} / C_{IC} \right)^{1/2} \quad . \tag{3.3}$$

Further, the dispersion relation of the disc-loaded coaxial structure which governs the propagation behavior of EM wave in different sections of the structure can be obtained using the relation [Dixit and Jain (2016)]:

$$\beta^2 - \omega^2 L_{IC} C_{IC} = 0 \quad . \tag{3.4}$$

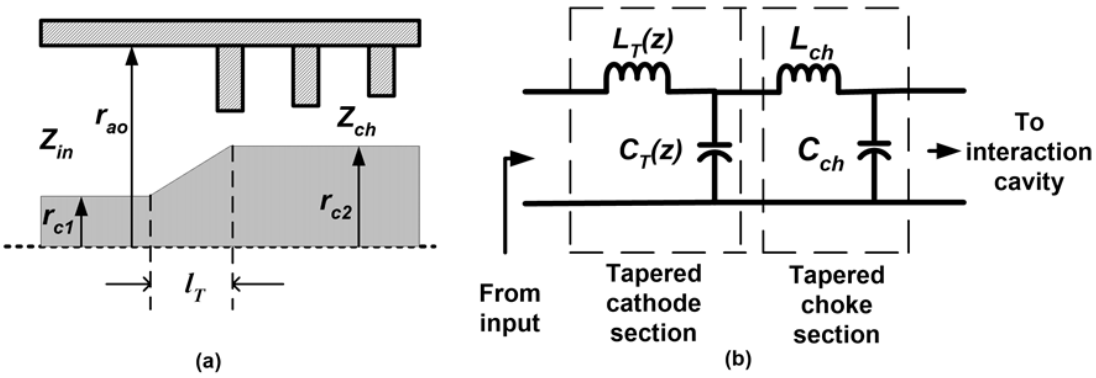

Figure 3.2: Input section of the MILO device (a) schematic, and (b) Equivalent circuit diagram.

3.3.1. Tapering towards the Input side of Cathode

This sub-section demonstrates the effect of tapering of the cathode at the input side. Tapering of cathode gradually changes the characteristic impedance along the axial direction (*z*-direction). The length of tapering should be chosen such that it should

match the input impedance of the device. Here, the tapered section of the cathode is used as the impedance matching section for the input section of the device. Fig. 3.2 shows the equivalent circuit diagram of the input side (section-A) of the device.

The two impedances, i.e. the coaxial section impedance (Z_{in}) and choke section impedance (Z_{ch}) should be matched. The tapered section inductance ($L_T(z)$) and capacitance ($C_T(z)$) can be calculated as follows [Chen (1966)]:

$$L_T(z) = L_0 f(z) \tag{3.5}$$

and

$$C_T(z) = C_0 f(z) \quad , \tag{3.6}$$

where $L_0 \left(= (\mu / 2\pi) \times \ln(r_{a0} / r_{c1})\right)$ and $C_0 \left(= 2\pi\varepsilon / \ln(r_{a0} / r_{c1})\right)$ are the inductance and capacitance per unit length of the input coaxial structure and *f(z)* (= r_{c1}+*az)*, *w*here *a* is the slope of the taper) is a linearly varying function with axial distance *z*. The optimum tapering length is required for the minimum reflection coefficient at the input side throughout the passband. The reflection coefficient (q_v) at any point along the tapered line defined by the first-order nonlinear differential equation [Walker and Lax (1946)]:

$$\frac{dq_v}{dz} - 2\Gamma(z) q_v + \frac{1}{2} \frac{d \log K(z)}{dz} (1 - q_v^2) = 0 \quad . \tag{3.7}$$

Here, $\Gamma(z)$ is the nominal propagation constant and $K(z)$ is the nominal characteristic impedance of the tapered line.

For the optimal design of the tapered section considering lossless condition, the solution of the above differential expression can be given as:

$$q_v = (q_{v,0}) e^{(-j\beta l_T)} \frac{\cos(\sqrt{(\beta l_T)^2 - A^2})}{\cosh(A)} \quad , \tag{3.8}$$

Here, β ($=2\pi/\lambda$) is the phase constant and A determines the maximum reflection allowed in the passband.

3.3.2. Tapered Choke Section

RF choke section at the input side is used to stop the RF leakage towards the high voltage DC pulser supply and also reduces in-phase reflection towards the main interaction cavity [Lemke *et al.* (1997)]. The choke section is designed in such a way that its cut-off frequency is lower than the cut-off frequency of the RF interaction cavities section. The choke inner radius is smaller than the inner radius of the RF interaction cavity discs. Due to a mismatch in the inner radius of the choke disc with the inner radius of RF interaction cavity discs, the impedance discontinuity occurs at the input section of the MILO device generating spurious emission of electrons from the cathode near this section [Fan *et al.* (2007)]. To overcome this problem, the device is designed with tapering of choke inner radius towards the input side. Tapering of choke radius gradually changes the characteristic impedance and helps in matching the impedance with the next section (i.e. RF interaction section) and improves RF selectivity of the choke section. It also helps the emitted electrons to reach closer to the interaction cavities [Jiang *et al.* (2017)]. Fig. 3.3 shows the equivalent circuit diagram for the tapered choke section of the MILO device.

The choke section characteristic impedance can be calculated using equivalent inductance and capacitance per unit length which mainly depends upon choke disc inner

radius and disc periodicity. The equivalent inductance per unit length $L_{ch}(z)$ and the equivalent capacitance per unit length $C_{ch}(z)$ in this section can be calculated using Eqs. (3.1) and (3.2), respectively, by replacing r_{ai} with r_{ch}. Similarly, the characteristic impedance of this section can be calculated using Eq. (3.3) by replacing L_{IC} with $L_{ch}(z)$ and C_{IC} with $C_{ch}(z)$.

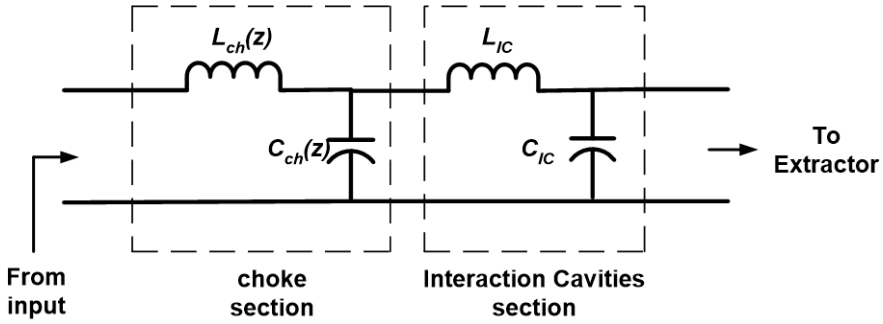

Figure 3.3: Equivalent circuit diagram of the MILO device at the input side**.**

3.3.3. Impedance Matching at the Extractor Section

Interaction between the electron beam and RF waves takes place in the RF interaction cavities (section-C, Fig. 3.1) region. In this region of the device, the axial electron velocity is made equal to the RF phase velocity while the group velocity is kept close to zero so that it gets a longer time for beam wave interaction. Thereby, electron bunches formation becomes denser and a larger part of beam energy can be transferred to the RF waves. As these waves come out from the interaction section, it should quickly move to the next section so that further signal growth can take place in the interaction section of the device. Therefore, we have to increase its group velocity, i.e. the standing waves of the interaction section have to be converted into traveling waves at the extractor region of the device which can be controlled by changing the extractor disc inner radius. The

impedance of this extractor section should match with the RF interaction section, which can be controlled by extractor cavity depth and extractor gap. Extractor gap forms capacitance which couples RF energy stored in the form of standing waves inside interaction structure towards the output end of the device [Friedman *et al.* (1990)]. The equivalent circuit diagram of the extractor part is shown in Fig. 3.4, where $C_{E.G}$, L_{ext} , and C_{ext} represent extractor gap capacitance, equivalent inductance per unit length, and equivalent capacitance per unit length of the extractor, respectively. The gap capacitance $C_{E.G}$ can be estimated with the help of the electric field intensity defined according to Gauss's law of electrostatics:

$$E_{E.G} = \sigma_{E.G} / \varepsilon_0 \quad , \tag{3.9}$$

where $\sigma_{E.G}$ represents the charge per unit length at the extractor disc-bottom surface and ε_0 is the permittivity of vacuum. Thus,

$$\sigma_{E.G} = \varepsilon_0 E_{E.G} = (\varepsilon_0 V_{E.G} / z) \ . \tag{3.10}$$

Here, *z* is the axial distance. The equivalent extractor gap capacitance can be calculated by the capacitance definition as:

$$C_{E.G} = (Q_{E.G} / V_{E.G}) \quad , \tag{3.11}$$

Where $Q_{E.G}$ is the surface charge at the extractor disc and can be given as [Fan *et al.* (2008)]:

$$Q_{E.G} = \int_{d_{ex}}^{d_{ex}+T} \sigma_{E.G} 2\pi R_{ext} dz = \int_{d_{ex}}^{d_{ex}+T} (\varepsilon_0 V_{E.G} / z) 2\pi R_{ext} dz \, . \tag{3.12}$$

Thus, using Eqs. (3.11) and (3.12), equivalent extractor gap capacitance can be estimated as:

$$C_{E.G} = 2\pi\varepsilon_0 R_{ext} V_{E.G} \ln\left((d_{ex} + T)/d_{ex}\right) . \quad (3.13)$$

The equivalent inductance per unit length (L_{ext}) of the extractor section can be calculated using Eq. (3.1) by replacing r_{ai} with r_{ext}. Similarly, the equivalent capacitance per unit length (C_{ext}) can be calculated using Eq. (3.2). The effective capacitance of the extractor part can be expressed as:

$$C_{ex} = (C_{ext} \times d_{ex}) + C_{E.G} \quad . \quad (3.14)$$

Similarly, effective inductance of the extractor section can be expressed as:

$$L_{ex} = L_{ext} \times d_{ex} . \quad (3.15)$$

Using the above two Eqs. (3.14) and (3.15), we can calculate effective characteristic impedance of extractor as:

$$Z_{ex} = (L_{ex}/C_{ex})^{1/2} \quad . \quad (3.16)$$

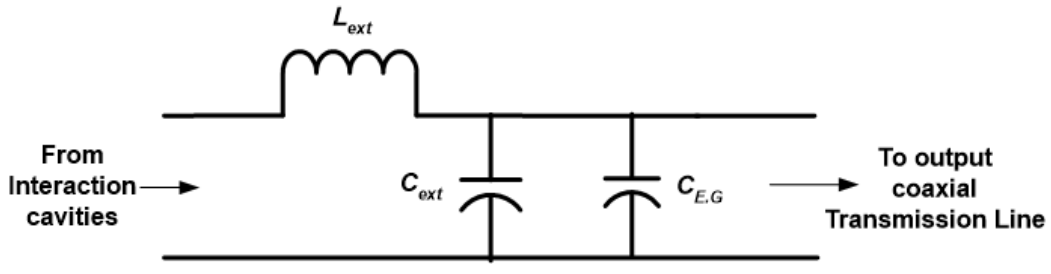

Figure 3.4: Equivalent circuit diagram of the extractor part of MILO.

3.3.4. Stub Position Optimization

MILO being an HPM source requires an efficient RF power extraction mechanism. Adjacent to the extraction section of the device is the stub section. The stub is to be optimally designed so that the RF power generated in the device can be efficiently coupled out. The stub section is also to be impedance matched with the output window of MILO. It also provides a return path to generate the load current essentially required for magnetic insulation of the device. Self-magnetic insulation of the MILO device is attained when the load current becomes equal to or greater than the critical current. It is having very low impedance and inductive in nature with impedance, $|Z_{stub}| = \omega L_{stub}$. The Inductance of stub rods can be approximated as:

$$L_{stub} \approx \frac{\mu l_{stub}}{8\pi} \quad . \tag{3.17}$$

Here, l_{stub} is the length of the stub. Stub works as DC short and RF open [Dixit *et al.* (2017)]. The inductance of the rods is large enough so that they do not perturb the axial radiation of the generated RF. It also provides support to the output coaxial transmission line. In conventional MILO design, six stubs are used which results in poor shot-to-shot reproducibility [Haworth *et al.* (2000)]. In order to eliminate this problem, six number of $\lambda/4$ stubs are replaced with four rods that are placed at a distance of $\lambda_g/4$. If the stubs are not placed properly, it causes reflection. Therefore, the location and radius of the stubs are selected in such a way to maximize the RF transmission with minimum reflection. The equivalent circuit analysis is carried out to find the reflection and transmission coefficient due to the stub position. An equivalent circuit diagram for the stub section is given in Fig. 3.5, where, a shunt stub is present at the distance *l* from the

input of the collector. The equivalent inductance per unit length L_{cx} and equivalent capacitance per unit length C_{cx} for the coaxial line are shown in Fig. 3.5 with stub at the center of the coaxial line. Here, the ABCD matrix is used to obtain the design expression, with electrical length taken as βl. The ABCD matrix for the cascaded structure of the T-shaped pattern can be written as [Zhang and Chen (2007)]:

$$\begin{bmatrix} A & B \\ C & D \end{bmatrix} = \begin{bmatrix} \cos(\beta l) & jZ_c \sin(\beta l) \\ \dfrac{j\sin(\beta l)}{Z_c} & \cos(\beta l) \end{bmatrix} \begin{bmatrix} 1 & 0 \\ \dfrac{j\tan(\beta l_{stub})}{Z_{stub}} & 1 \end{bmatrix} \begin{bmatrix} \cos(\beta l) & jZ_c \sin(\beta l) \\ \dfrac{j\sin(\beta l)}{Z_c} & \cos(\beta l) \end{bmatrix} \tag{3.18}$$

Here, $Z_c = \sqrt{L_{cx} / C_{cx}}$ is the characteristic impedance of the output coaxial structure. After solving for the matrix of the above equation we get:

$$A = D = \cos^2(\beta l) - \sin^2(\beta l) - \frac{Z_c \sin(\beta l)\cos(\beta l)\tan(\beta l_{stub})}{Z_{stub}} \quad , \tag{3.19}$$

$$B = 2jZ_c \sin(\beta l)\cos(\beta l) - j\frac{Z_c^2 \sin^2(\beta l)\tan(\beta l_{stub})}{Z_{stub}} \tag{3.20}$$

$$C = \frac{2j\sin(\beta l)\cos(\beta l)}{Z_c} + \frac{j\cos^2(\beta l)\tan(\beta l_{stub})}{Z_{stub}} \quad . \tag{3.21}$$

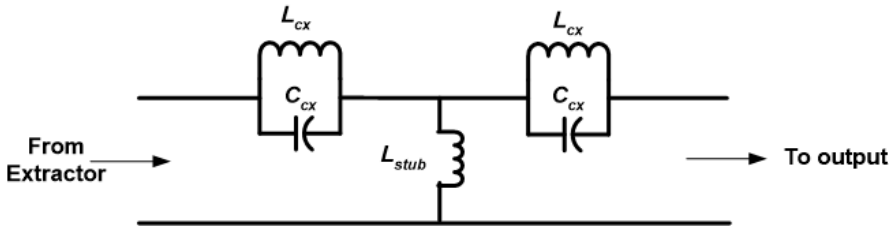

Figure 3.5: Equivalent circuit diagram for the stub section.

Changing the ABCD matrix to that of the scattering matrix can be written as [Orfanidis (2013)]:

$$[S]=\frac{1}{A_t}\begin{bmatrix} A+\frac{B}{Z_0}-CZ_0-D & 2(\mathrm{AD}-\mathrm{BC}) \\ 2 & -A+\frac{B}{Z_0}-CZ_0-D \end{bmatrix} \tag{3.22}$$

where, $A_t = A+B/Z_0+CZ_0+D$ and Z_0 is the characteristic impedance of vacuum with which the stub has to match the impedance.

3.4. Results and Discussion

MILO is a giga-watt class of oscillator which operates with self-magnetic insulation condition. The device essentially requires design parameters optimization so that all the device sub-sections are impedance matched from the input to the output end of the MILO device. Power transfer between low to high impedance causes reflection and forms the standing wave which results in power loss. Impedance matching is important for minimizing this reflection and maximizing the power transfer from source to load. The analysis described in the preceding section can be readily used for finding as well as matching the impedances of the different subsections of the device. To validate the analysis and understand the effect of impedance matching at the different sections, the experimental design parameters for an *L*-band MILO [Lemke *et al.* (1997)], given in table 3.1 have been taken. Further, in the following section, the optimization of the different device sub-sections are demonstrated adapting the above analytical procedure and modified device design parameters are listed in table 3.1.

Table 3.1: Typical L-band MILO specification.

(a) Electrical specification		
Particular	**Specification [Lemke *et al.* (1997)]**	**Modified**
Voltage(V)	510 kV	510 kV
Current (I)	34 kA	34 kA
Operating Frequency	1.18 GHz	1.18 GHz
(b) Structural specification		
Cathode Radius (r_c)	57.5 mm	Tapered: 28.5 mm-57.5 mm
Anode Radius (r_{ao})	143mm	143 mm
SWS disc inner Radius (r_{ai})	86 mm	86 mm
Extractor vane Radius (r_{ex})	89 mm	89 mm
Choke disc Radius (r_{ch})	76 mm	76 mm, 79 mm, 82 mm
Disc Thickness (T)	10 mm	10 mm
Periodicity (d)	38.4 mm	41.6 mm
Extractor gap (d_{ex})	-	63 mm

3.4.1. Optimization of the Tapering Length of the Cathode at the Input Side

Tapering the input side of the cathode is used for matching the two different unequal impedances over the desired frequency band. The device input section uses a coaxial line, usually having a standard impedance value. Choke section impedance should also match with DC power supply impedance. The characteristic impedance of the choke section is calculated using Eqs. (3.3). Matching of these two unequal impedances minimizes reflections at this section of the device and is achieved by proper selection of

taper length. Fig. 3.6 shows the magnitude of reflection with normalized tapered length. It can be seen from Fig. 3.6 that for the optimum tapered length, an odd multiple of λ/4 is required where reflection magnitude becomes minimum.

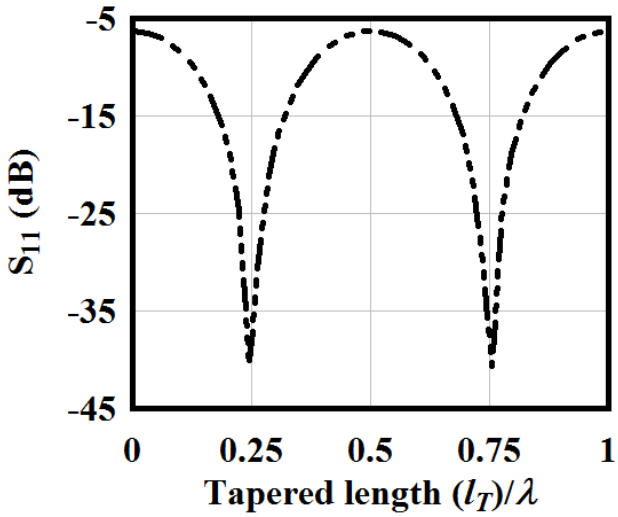

Figure 3.6: Reflection coefficient (S_{11}) with normalized tapered length at the input side.

3.4.2. Optimization of tapered choke section

The choke section is used to block the back wave propagation of RF waves from RF interaction cavities section (section-C, Fig. 3.1) towards the input side of the device by lowering the cut-off frequency of the choke cavities. The cut-off frequency of the choke section depends upon the choke radius and disc periodicity, which can be calculated using Eqs. 3.4. The cut-off frequency of the choke section is generally, taken as ~ 80% of the operating frequency of the device.

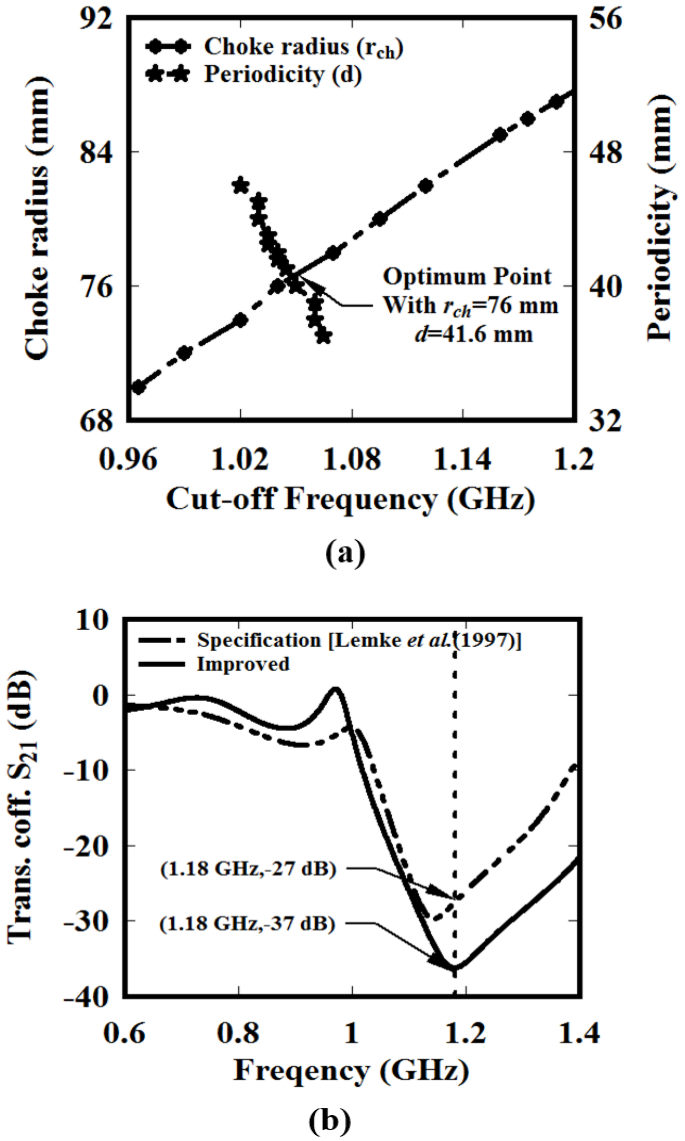

Figure 3.7: (a) Choke section optimization with cut-off frequency (b) Transmission coefficient at the choke section comparison with two designs.

Tapering of choke radius gradually decreases the cut-off frequency and helps in matching the impedance with the RF interaction section. Fig. 3.7(a) shows the cut-off frequency for different choke radius and different periodicity. At the optimum choke radius and periodicity, the transmission coefficient (S_{21}) at the choke section is shown in Fig. 3.7(b). It can be seen from Fig. 3.7(b) that the optimum design parameter provides the improved response.

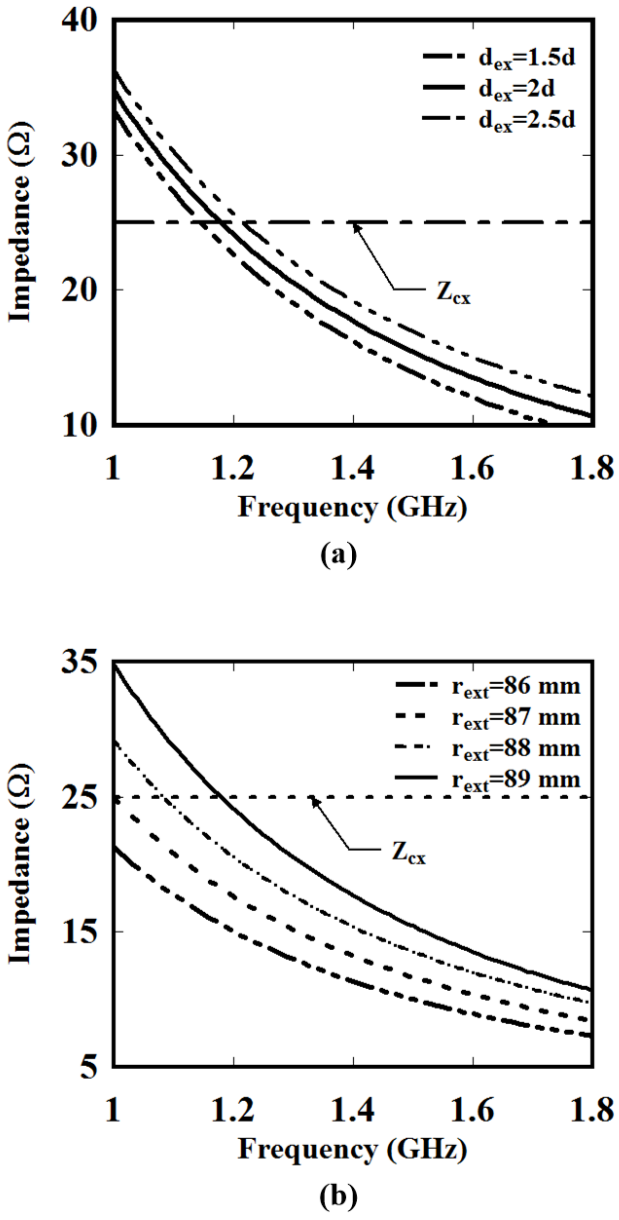

Figure 3.8: Extractor part characteristic impedance at a different frequency (a) at different extractor gap (b) at different extractor radius.

3.4.3. Optimization of Extractor Section

The extractor part including the extractor disc and extractor gap is used to transform the impedance of SWS to that of the output section. Fig. 3.8 shows the characteristic impedance for the output section of the device. Fig. 3.8 (a) shows the characteristic

impedance of the extractor section at different extractor gaps with different frequencies. It can be observed from Fig. 3.8 (a), that the extractor gap does not have much effect on the characteristic impedance of the extractor section. With a larger extractor gap, the electric field matching reduces at the collector end and vice versa. Fig. 3.8 (b) shows the characteristic impedance of the extractor at different disc inner radius. It can be observed from the Fig. 3.8 (b) that with the increase in the extractor radius, the impedance of the extractor part increases. Fig. 3.9 (a) indicates the reflection coefficient at the output side of the MILO device. The minimum reflection of (~ -35dB) of RF is observed at operating frequency (1.18 GHz) with the optimum extractor design parameter. This explains that the maximum power can be extracted out from the device through the impedance matching of the RF interaction cavity section with the output coaxial transmission line through extractor section optimization.

To demonstrate the electromagnetic wave synchronism with the different sections of the MILO device, the dispersion plot is shown in Fig. 3.9(b). It can be observed from Fig. 3.9(b) that the choke section filters out the RF wave propagation from the interaction cavities towards the input side by reducing the cut-off frequency. Similarly, the extractor section dispersion relation shows that it changes the group velocity by changing the slope of the dispersion curve at the operating frequency. The group velocity of the RF near the interaction section is $0.025\times c$ which changes to $0.16\times c$ near the extractor section. The positive value of group velocity implies the movement of energy in the forward direction whereas the negative value of group velocity implies a movement of energy in the backward direction.

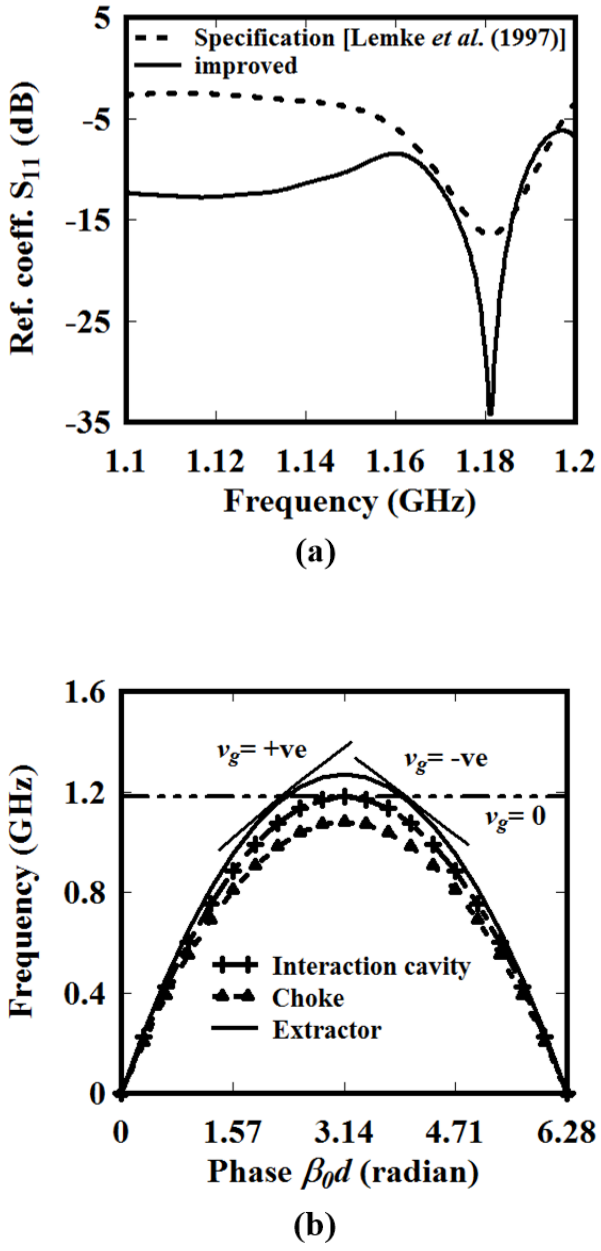

Figure 3.9: (a) Reflection coefficient at the output side (b) Dispersion relation of fundamental mode for the different sections of the device.

3.4.4. Optimization of Stub Position

The stub is used to provide mechanical support to the collector and as well as to provide a return path for the load current. To optimize the stub position, as explained in

preceding section 3.3.4, it is optimally designed and Eqs. (3.18) is used for calculating the reflection coefficient (S_{11}) for different stub position. Fig. 3.10 shows the reflection coefficient (S_{11}) for different positions of the stub from the extractor disc. It can be seen from Fig. 3.10 that at $(2n+1)\lambda_g / 4$ distance from the extractor, minimum reflection can be obtained from the stub. Thus, to improve the efficiency of the MILO device the optimum position of the stub should be at the odd multiple of $\lambda_g / 4$.

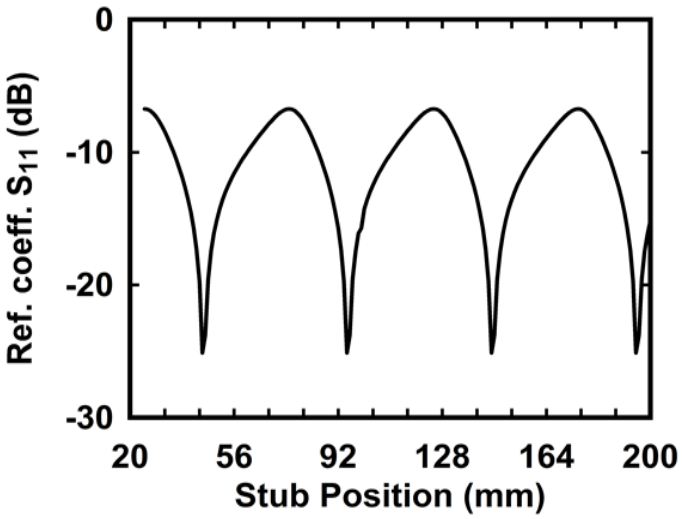

Figure 3.10: Reflection coefficient for stub section with different positions from the extractor disc.

3.4.5 Simulation Results

In order to validate the design parameters, the dispersion diagram has been plotted using Eq. (3.7) with the parameters given in Table 3.1. To evaluate the performance improvement of the MILO device by optimizing the different section adapting the method described in section 3.3, 3D PIC simulation of an experimental *L*-band MILO oscillator reported in [Lemke *et al.* (1997)] is performed reconfiguring a commercial code "CST Studio Suite". The beam present (hot) simulation is performed for a single

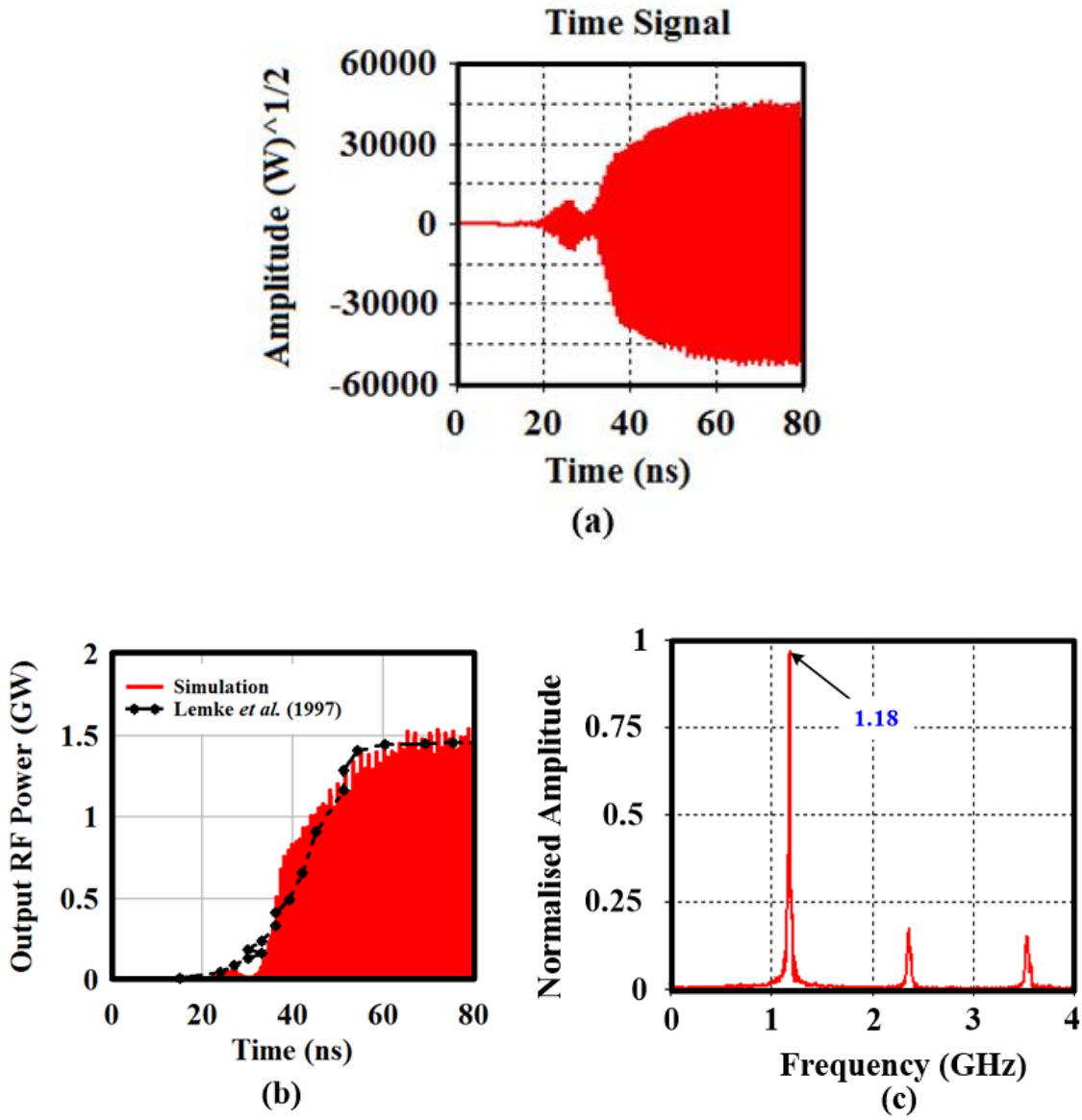

Figure 3.11: (a) Output RF signal received at the output port, (b) RF output power developed at the output port with experimental data (c) FFT of the generated signal at the output port.

pulse of 80 ns, using beam parameters: 510 kV voltages and 34 kA current. The generated RF signal received at the output port is shown in Fig. 3.11 (a). The maximum output RF power (obtained through $(\text{Amplitude}^2)/2$) of the RF signal) with peak value 1.38 GW and efficiency of ~7.8% obtained with the reported design parameters and it is

found ~5% in agreement with the reported experimental results [Lemke *et al.* (1997)] shown in Fig. 3.11(b). The corresponding FFT of the signal shown in Fig. 3.11 (c) confirms the oscillation frequency of 1.18 GHz.

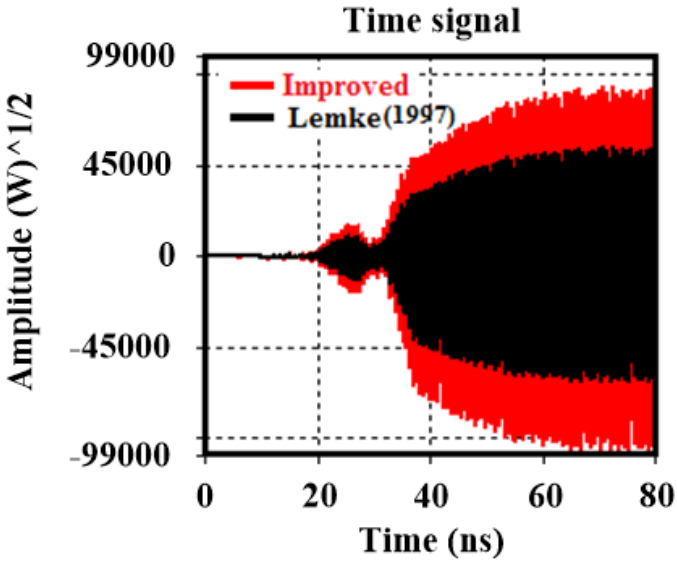

Figure 3.12: Output RF signal received at the output port comparison.

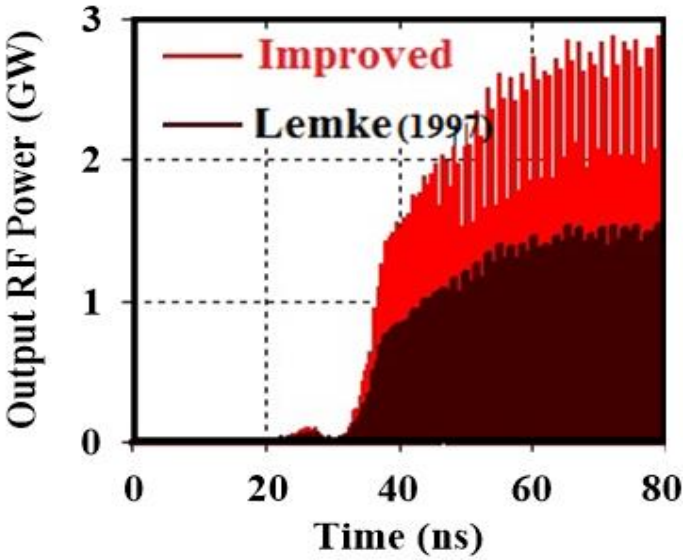

Figure 3.13: RF output power developed at the output port with improvement in the device structure.

The RF signal generated at the output port with literature [Lemke *et al.* (1997)] specification and as per improved design are shown in Fig. 3.12. It can be seen from Fig. 3.12 that with the optimized design parameter the RF signal amplitude increases by 50%, resulting in better performance. After implementing the overall impedance matching of the device at the input side with cathode tapering and at the output side with an optimum extractor gap, the maximum RF power transfer to the output side at 1.18 GHz. With the improvement in design at the input as well as output section, the output RF power of 2.5 GW is obtained with an efficiency of ~14.4%. The improved output temporal RF power compared with the reported results is shown in Fig. 3.13.

3.5. Conclusion

MILO is an HPM oscillator and its design is optimized for performance improvement. The device performance improvement and optimization studies are explored here by adapting the impedance matching approach of its different sections. For this purpose, circuit impedances are evaluated in terms of their equivalent circuit parameters, equivalent shunt capacitance, and equivalent series inductance per unit circuit length. This approach is much easier and simple to handle compared to the field analytical approach.

The standard reported characteristic impedance results of the MILO structure are used for impedance matching the input and output section of the MILO device and are analyzed using an equivalent circuit approach. Input impedance matching depends upon cathode tapering length at the input side. The optimum tapering length found an odd multiple of $\lambda/4$. Similarly, the output section impedance matching depends upon the extractor section by varying extractor gap. Extractor radius changes group velocity of

RF from 0.025c to 0.16c. Further, the optimization of the stub position is described. To validate the performance improvement of the MILO device, a 3D PIC simulation is performed for a reported experimental device operating at 510 kV voltages and 34 kA of beam current. The RF output power of 1.38 GW with an efficiency of 7.8% is obtained and it is found to be in agreement within 5%. Further, the simulation is carried out for the device with an optimized design parameter obtained through analytical study. The RF output power is increased to 2.5 GW with an efficiency of 14.4%.